THE JOURNAL OF BIOLOGICAL CHEMISTRY VOL. 291, NO. 5, pp. 2319–2330, January 29, 2016

Epiregulin Recognition Mechanisms by Anti-epiregulin Antibody 9E5

*STRUCTURAL, FUNCTIONAL, AND MOLECULAR DYNAMICS SIMULATION ANALYSES**

Received for publication, April 2, 2015, and in revised form, November 23, 2015 Published, JBC Papers in Press, December 1, 2015, DOI 10.1074/jbc.M115.656009

Yuji Kado[‡§1], Eiichi Mizohata[‡1], Satoru Nagatoishi[¶1], Mariko Iijima[‖], Keiko Shinoda[‖2], Takamitsu Miyafusa[¶], Taisuke Nakayama[‡], Takuma Yoshizumi[‡], Akira Sugiyama[‖], Takeshi Kawamura[‖], Young-Hun Lee[‖], Hiroyoshi Matsumura[‡3], Hirofumi Doi[‖], Hideaki Fujitani[‖2], Tatsuhiko Kodama[‖], Yoshikazu Shibasaki[‖], Kouhei Tsumoto[¶4], and Tsuyoshi Inoue[‡5]

From the [‡]Division of Applied Chemistry, Graduate School of Engineering, Osaka University, 2-1 Yamada-Oka, Suita, Osaka 565-0871, Japan, [§]Interdisciplinary Program for Biomedical Sciences, Institute for Academic Initiatives, Osaka University, 1-1 Yamadaoka, Suita, Osaka 565-0871, Japan, [¶]Medical Proteomics Laboratory, The Institute of Medical Science, The University of Tokyo, 4-6-1 Shirokanedai, Minato-ku Tokyo 108-8639, Japan, and [‖]Laboratory for Systems Biology and Medicine, Research Center for Advanced Science and Technology, The University of Tokyo, 4-6-1 Number 34 Komaba, Meguro-ku, Tokyo 153-8904, Japan

Epiregulin (EPR) is a ligand of the epidermal growth factor (EGF) family that upon binding to its epidermal growth factor receptor (EGFR) stimulates proliferative signaling, especially in colon cancer cells. Here, we describe the three-dimensional structure of the EPR antibody (the 9E5(Fab) fragment) in the presence and absence of EPR. Among the six complementarity-determining regions (CDRs), CDR1–3 in the light chain and CDR2 in the heavy chain predominantly recognize EPR. In particular, CDR3 in the heavy chain dramatically moves with cis-trans isomerization of Pro^{103}. A molecular dynamics simulation and mutational analyses revealed that Arg^{40} in EPR is a key residue for the specific binding of 9E5 IgG. From isothermal titration calorimetry analysis, the dissociation constant was determined to be 6.5 nM. Surface plasmon resonance analysis revealed that the dissociation rate of 9E5 IgG is extremely slow. The superimposed structure of 9E5(Fab)·EPR on the known complex structure of EGF·EGFR showed that the 9E5(Fab) paratope overlaps with Domains I and III on the EGFR, which reveals that the 9E5(Fab)·EPR complex could not bind to the EGFR. The 9E5 antibody will also be useful in medicine as a neutralizing antibody specific for colon cancer.

Recently, antibody therapy has been attracting considerable attention as a possible cure for several types of diseases. For instance, trastuzumab is a humanized IgG1κ monoclonal antibody that is targeted for the human epidermal growth factor (EGF) receptor (EGFR)[6] 2 (HER2, ErbB-2), which is used in the treatment of metastatic breast cancer (1).

Initially, the EPR precursor protein is expressed as a type I transmembrane protein. A disintegrin and metalloproteinase 17 (ADAM17) catalyzes ectodomain shedding of the EPR precursor protein, which produces mature EPR (2). EPR induces dimerization of EGFR and promotes autophosphorylation in the intracellular kinase domain of EGFR (3). EGFR phosphorylation activates several types of intracellular signaling pathways, such as the mitogen-activated protein kinase (MAPK), phosphoinositide 3-kinase (PI3K)/Akt, and STAT5 pathways (4–6). As a result, proliferation, cell survival, and angiogenesis are induced in the cell.

Although the expression of EPR is suppressed in most adult normal tissues, EPR is overexpressed in human colon, breast, and ovarian cancers (7–10). Therefore, normalization of EGF signaling is expected to cure these cancers. Recently, humanized anti-EPR antibodies with high affinity targeted cytotoxicity have been prepared and characterized (11), and these antibodies have the potential to act as anticancer drugs.

The structure of EPR was first determined by NMR (12). Similar to the other EGF family ligands, EPR (residues Val^{1}–Leu^{46}) is composed of an N-terminal domain (residues Ile^{3}–Glu^{33}) that has a β-hairpin motif called the core region (residues Gly^{17}–Cys^{32}) and a C-terminal domain (residues Val^{34}–Phe^{45}). Three disulfide bridges stabilize the entire EPR structure. For the EGF family antibody ligand, the structures of transforming growth factor β complexed with Fab or single chain Fv of fresolimumab have been reported (13).

* This work was supported in part by the Funding Program for World-Leading Innovative Research and Development on Science and Technology (FIRST Program), the Creation of Innovation Centers for Advanced Interdisciplinary Research Areas Program, and Ministry of Education, Culture, Sports, Science and Technology (MEXT)/Japan Society for the Promotion of Science Grants-in-aid for Scientific Research (KAKENHI) 24770096 and 25282230. The authors declare that they have no conflicts of interest with the contents of this article.

The atomic coordinates and structure factors (codes 5AZ2 and 5E8D) have been deposited in the Protein Data Bank (http://wwpdb.org/).

[1] These authors contributed equally to this work.

[2] Supported in part by MEXT Strategic Programs for Innovative Research Supercomputational Life Science Grants hp130006 and hp140228.

[3] Present address: College of Life Sciences, Ritsumeikan University, 1-1-1 Nojihigashi, Kusatsu, Shiga 525–8577, Japan.

[4] To whom correspondence may be addressed. Tel.: 81-3-5449-5316; Fax: 81-3-6409-2127; E-mail: tsumoto@ims.u-tokyo.ac.jp.

[5] To whom correspondence may be addressed. Tel.: 81-6-6879-7408; Fax: 81-6-6879-7409; E-mail: inouet@chem.eng.osaka-u.ac.jp.

[6] The abbreviations used are: EGFR, epidermal growth factor receptor; EPR, epiregulin; Fab, fragment, antigen binding; CDR, complementarity-determining region; F_v, variable region of Fab; V_H, variable region of a heavy chain; V_L, variable region of a light chain; C_L, constant region of a light chain; C_{H1}, constant region of a heavy chain; r.m.s.d., root mean square deviation; MD, molecular dynamics; ITC, isothermal titration calorimetry; SPR, surface plasmon resonance; hEPR, EPR from *H. sapiens*; mmEPR, EPR from *M. musculus*; K_A, association constant; K_D, dissociation constant; ΔH, binding entropy; ΔS, binding entropy; ΔG, Gibbs free energy; m3, triple mutant E27Q/K28N/F29Y.

To design an effective humanized antibody, we investigated the antibody recognition mechanism between mature EPR and the 9E5(Fab) fragment by x-ray structural analysis. In this study, we describe the three-dimensional structure of the 9E5(Fab) fragment with and without EPR. Moreover, a molecular dynamics (MD) simulation, isothermal titration calorimetry (ITC), and surface plasmon resonance (SPR) analysis were performed to clarify the structure-function relationship. These findings are expected to aid in the development of future drugs, especially those that target cancers.

Experimental Procedures

Production and Purification of 9E5(Fab)—The 9E5 monoclonal antibody was produced using a method described previously (11). Hybridoma cells were intraperitoneally implanted in BALB/c nude mice (BALB/cSlc-nu/nu), and ascites were obtained from the mice and examined with a Bio-Scale Mini UNOsphere SUPrA cartridge (Bio-Rad). The peak fractions were injected into a Bio-Scale Mini Bio-Gel P-6 (Bio-Rad).

To prepare 9E5(Fab), the Fc fragments of 9E5 IgG released by papain digestion (9E5 IgG:papain, 100:1) were used. The digested samples were loaded onto a Bio-Scale CHT5-I column (Bio-Rad) and eluted with a linear gradient of 0.5–250 mM sodium phosphate buffer (pH 6.8). The peak fractions were collected and concentrated, and they were then injected onto a HiLoad 16/60 Superdex 75 prep grade column (GE Healthcare), which was developed with 20 mM Tris-HCl (pH 7.5) buffer containing 300 mM NaCl. The peak fractions containing 9E5(Fab) were collected and concentrated to 10 mg ml^{-1} by ultrafiltration with Vivaspin (10-kDa cutoff; GE Healthcare).

Construction of the EPR Expression Plasmids—We constructed EPR from *Homo sapiens* (hEPR) and *Mus musculus* (mmEPR) pro-EPR cDNA (residues 1–46), which is elongated by 24 residues toward the N terminus (residues −23 to 46) to improve its fusibility. The EPR gene was cloned into a modified pET32a vector (Novagen, Billerica, MA), which was in-frame with a hexahistidine tag, thioredoxin, and the HRV3C protease cleavage site at the N terminus.

Site-directed mutagenesis was performed with PCR mutagenesis. In hEPR, the following oligonucleotide primer pairs were used (the mutated sites are underlined): D9A forward, 5′-TCACCAAATGTTCTAGCGCAATGAATGGTTATTGTCT-3′; D9A reverse, 5′-AGACAATAACCATTCATTGCGCTAGAACATTTGGTGA-3′; S26R forward, 5′-GTATCTATCTGGTTGACATGCGTCAGAATTATTGTCGTTGCGA-3′; S26R reverse, 5′-TCGCAACGACAATAATTCTGTGCCATGTCAACCAGATAGATAC-3′; R40A forward, 5′-TCGGTTACACCGGCGTCGCATGCGAGCACTTCTTCCT-3′; and R40A reverse, 5′-AAGAAGTGCTCGCATGCGACGCCGGTGTAACCGA-3′. In mmEPR, the following designed primer pairs were used: R26S forward, 5′-TATCTACCTGGTCGATATGTCTGAGAAATTCTGTCGTTGTG-3′; R26S reverse, 5′-CACAACGACAGAATTTCTCAGACATATCGACCAGGTAGATA-3′; E27Q/K28N/F29Y forward, 5′-CTACCTGGTCGATATGCGTCAGAACTACTGTCGTTGTGAGGTTGGTT-3′; and E27Q/K28N/F29Y reverse, 5′-AACCAACCTCACAACGACAGTAGTTCTGACGCATATCGACCAGGTAG-3′.

Expression and Purification of Recombinant EPRs—*Escherichia coli* SHuffle T7 cells (New England Biolabs, Ipswich, MA) were transformed with the prepared plasmids. The cells were cultured in lysogeny broth containing 100 μg ml^{-1} ampicillin at 37 °C until the optical density at 600 nm reached 0.6. The temperature was lowered to 15 °C, and then 0.4 mM isopropyl 1-thio-β-D-galactopyranoside was added to induce protein expression. After 24 h of cultivation, the cells were collected and stored at −80 °C until further use.

The cells were thawed and disrupted with an EmulsiFlex-C3 homogenizer (Avestin Inc., Ottawa, Canada) in 20 mM Tris-HCl buffer (pH 8.0) containing 500 mM NaCl, 20 mM imidazole, and 2500 units of Benzonase. After removal of the cell debris by centrifugation, the supernatant was applied to an nickel-nitrilotriacetic acid Superflow (Qiagen, Hilden, Germany) column and eluted with 20 mM Tris-HCl buffer (pH 8.0) containing 500 mM NaCl and 500 mM imidazole. HRV3C protease was added to the eluate, and it was dialyzed against dialysis buffer (20 mM Tris-HCl (pH 7.5) containing 600 mM NaCl). To remove the HRV3C protease and uncleaved fusion proteins, the dialyzed sample was applied to GS Trap and His Trap columns (GE Healthcare), and the flow-through fraction was recovered. The sample was concentrated and loaded onto a gel filtration chromatograph with a Hi-Load 16/60 Superdex 75 prep grade column, which was developed with the dialysis buffer. The fractions containing the EPR protein were buffer-exchanged into 20 mM Tris-HCl (pH 7.5) containing 300 mM NaCl and concentrated to 10 mg ml^{-1}.

X-ray Crystallography—The entire crystallization was performed with the sitting drop vapor diffusion method with a VIORAMO 96-well protein crystallization plate (Azone, Edobori, Osaka, Japan). For the crystallization of 9E5(Fab), 0.5 μl of protein solution (10 mg ml^{-1} 9E5(Fab), 20 mM Tris-HCl (pH 7.5), and 300 mM NaCl) was mixed with 0.5 μl of reservoir solution (50 mM HEPES-Na (pH 7.3) and 21.5% (v/v) polyethylene glycol (PEG) 4000) and incubated at 20 °C. Crystals of 9E5(Fab) formed within 7 days. For x-ray data collection, a 9E5(Fab) crystal was soaked in cryoprotectant solution (50 mM HEPES-Na (pH 7.3), 24% (v/v) PEG 4000, and 10% (v/v) glycerol) and flash frozen in liquid nitrogen.

For crystallization of the 9E5(Fab)·hEPR complex, 0.5 μl of protein solution (10 mg ml^{-1} 9E5(Fab)·hEPR, 20 mM Tris-HCl (pH 7.5), and 300 mM NaCl) was mixed with 0.5 μl of reservoir solution (100 mM MES monohydrate (pH 6.0) and 14% (v/v) PEG 4000) at 20 °C. The 9E5(Fab)·hEPR complex crystal formed within 7 days. For data collection, a 9E5(Fab)·hEPR crystal was soaked in cryoprotectant solution (100 mM MES monohydrate (pH 6.0), 17% (w/v) PEG 4000, and 20% (v/v) glycerol) and then flash frozen in liquid nitrogen.

The x-ray diffraction data sets for the 9E5(Fab) and 9E5(Fab)·hEPR complex crystals were collected at Photon Factory BL-5A and SPring-8 BL44XU, respectively. The diffraction data were integrated and scaled with HKL2000 (14). The structure of 9E5(Fab) was determined by the molecular replacement method using 82D6A3, which is an antithrombotic antibody (15) (Protein Data Bank code 2ADF), as the starting model with PHASER (16). To determine the 9E5(Fab)·hEPR complex structure, molecular replacement was performed with PHASER

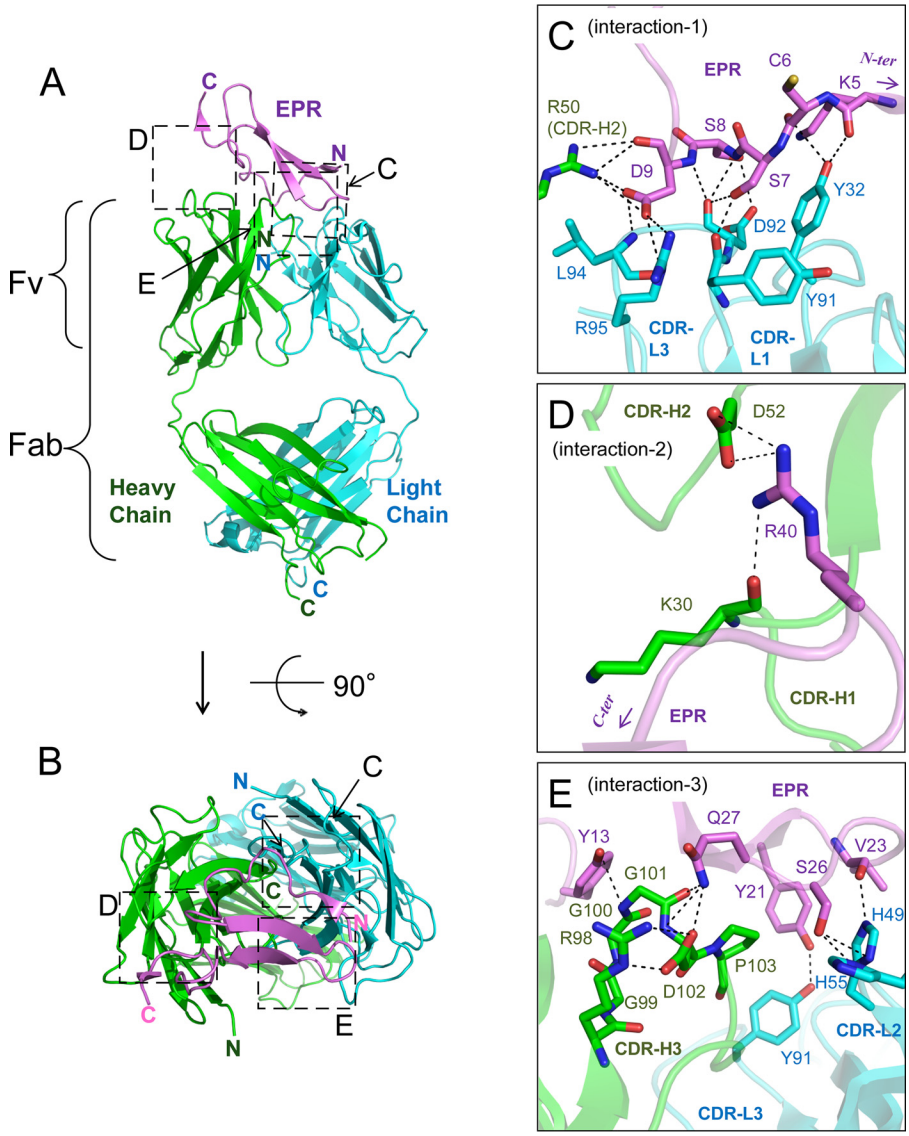

FIGURE 1. **Overall structure of the 9E5(Fab)·hEPR complex.** *A*, front view of the 9E5(Fab)·hEPR complex. hEPR and the heavy and light chains of 9E5(Fab) are colored *pink*, *green*, and *cyan*, respectively. *B*, top view of the complex structure. The *black dotted squares* in *A* and *B* show the locations of interaction-1 (enlarged in *C*), interaction-2 (enlarged in *D*), and interaction-3 (enlarged in *E*). *C*, interaction between CDR-L1, CDR-L3, and CDR-H2 in 9E5(Fab) and the N-terminal domain of hEPR (interaction-1). *D*, interaction between CDR-H1 and CDR-H2 in 9E5(Fab) and the C-terminal region of hEPR (interaction-2). *E*, interaction between CDR-L2 and CDR-H3 in 9E5(Fab) and the core region of hEPR (interaction-3). In *C*, *D*, and *E*, oxygen, nitrogen, and sulfur atoms are shown in *red*, *blue*, and *yellow*, respectively. Hydrogen bonds and salt bridges are shown as *black dashed lines*.

using the refined 9E5(Fab) structure and the NMR structure of hEPR (Protein Data Bank code 1K37) as the search models (12). Model building was performed using Coot (17), and the structure was refined using REFMAC5 (18) and PHENIX (19); 5% of the reflections were set aside for R_{free} calculations (20). The quality of the models was assessed with Ramachandran plots, and model geometry analyses were conducted with Rampage (21). All of the structural figures were drawn with PyMOL (22). The data collection and refinement statistics are summarized in Table 1.

Molecular Dynamics Simulations—All of the simulations were performed with the GROMACS 4.6.1 package (23–25) using the Fuji force field (26) for proteins, AMBER force field for ions, and TIP3P water potential. Na^+ and Cl^- ions were added to produce a neutral solution of 0.15 M. The Nosé-Hoover thermostat (27, 28) with a relaxation time of 1 ps was used to keep the solutions at 298 K. The Parrinello-Rahman scheme (29) was used as a barostat at 1 atm with a relaxation time of 1 ps. The simulation time step was 3 fs, and all of the bond lengths of the proteins were constrained using the LINCS algorithm (30). The leap-frog algorithm was used to integrate the equations of motion, and the particle mesh Ewald method (31) was used to calculate the electrostatic interactions with a real space cutoff of 1.0 nm. The neighbor list cutoff was also set at 1.0 nm. The initial structure was taken from our x-ray crystal structure of the complex. After energy minimization, the heavy atoms of the protein were restrained for 200 ps using a harmonic potential with a force constant of 1000 kJ^{-1} nm^{-2} to relax the water molecules. Four NPT (constant number of particles, pressure, and temperature) simulations were then performed for 1 s with initial random velocities that obeyed a Maxwell-Boltzmann distribution at 298 K.

TABLE 1
Data collection and refinement statistics for 9E5(Fab) and the 9E5(Fab)·EPR complex

	9E5(Fab)	9E5(Fab)·hEPR complex
Data collection		
X-ray source	Photon Factory BL5a	SPring-8 BL44XU
Detector	ADSC Quantum 210r	Rayonix MX-225HE
Wavelength (Å)	1.0000	1.0000
Space group	$P2_1$	$I222$
Unit-cell parameters (Å; °)	$a = 41.00$, $b = 79.83$, $c = 59.98$; $\beta = 92.59$	$a = 68.60$, $b = 100.29$, $c = 187.37$
Resolution range (Å)	50.00–1.60 (1.66–1.60)	50.00–2.50 (2.59–2.50)
Total no. of reflections	192,615	100,371
No. of unique reflections	48,127	22,299
$I/\sigma(I)$	16.2 (2.8)	28.9 (2.9)
Redundancy	4.0 (3.6)	4.5 (3.0)
Completeness (%)	95.3 (98.8)	97.3 (93.4)
R_{merge} [a] (%)	6.9 (34.9)	5.1 (30.9)
Refinement statistics		
Resolution (Å)	17.27–1.60	14.91–2.50
No. of reflections	46,334	22,005
R_{cryst} [b]/R_{free} [c] (%)	19.2/23.7	18.9/26.3
Mean Wilson B value (Å^2)	21.2	59.6
No. of non-H-atoms	3,627	3,660
r.m.s.d. from ideal values		
Bond lengths (Å)/angles (°)	0.007/1.181	0.009/1.329
Ramachandran statistics (%)		
Favored	97.2	93.5
Allowed	2.8	5.9

[a] $R_{merge} = \Sigma_i\Sigma_h|I_{hi} - I_h|/\Sigma_i\Sigma_h I_h$.
[b] $R_{cryst} = \Sigma||F_o| - |F_c||/\Sigma|F_o|$ calculated from 95% of the data, which were used during the course of the refinement.
[c] $R_{free} = \Sigma||F_o| - |F_c||/\Sigma|F_o|$ calculated from 5% of the data, which were used during the course of the refinement.

TABLE 2
Hydrogen bonds and salt bridges between 9E5(Fab) and hEPR (distance <3.5 Å)
Interaction-1, -2, and -3 correspond to the regions shown by Fig. 1, *C*, *D*, and *E*, respectively.

Interaction part	hEPR		9E5(Fab)			Interaction distance
	Residue	Atom	Residue	CDR	Atom	
						Å
Interaction-1	Lys^5	O	Tyr^{32}	L1	Oη	3.1
	Cys^6	O	Tyr^{32}	L1	Oη	3.5
	Ser^7	Oγ	Tyr^{91}	L3	O	2.5
	Ser^7	Oγ	Asp^{92}	L3	O	3.1
	Ser^8	N	Asp^{92}	L3	O	3.2
	Ser^8	Oγ	Asp^{92}	L3	Oδ1	3.2
	Asp^9	N	Asp^{92}	L3	O	3.1
	Asp^9	Oδ1	Leu^{94}	L3	N	3.2
	Asp^9	Oδ2	Arg^{95}	L3	Nϵ	3.2
	Asp^9	Oδ2	Arg^{95}	L3	Nη2	3.3
	Asp^9	Oδ1	Arg^{50}	H2	Nη1	3.0
	Asp^9	Oδ2	Arg^{50}	H2	Nη1	3.5
	Asp^9	O	Arg^{50}	H2	Nη1	3.4
	Asp^9	O	Arg^{50}	H2	Nη2	3.4
Interaction-2	Arg^{40}	Nη1	Lys^{30}	H1	O	3.3
	Arg^{40}	Nη1	Asp^{52}	H2	Oδ1	2.8
	Arg^{40}	Nη2	Asp^{52}	H2	Oδ2	3.5
Interaction-3	Tyr^{13}	Oη	Gly^{101}	H3	N	3.3
	Tyr^{21}	Oη	Tyr^{91}	L3	Oη	2.6
	Val^{23}	O	His^{49}	L2	Nϵ2	2.7
	Ser^{26}	Oγ	His^{49}	L2	Nδ1	3.5
	Ser^{26}	Oγ	His^{55}	L2	Nδ1	3.1
	Gln^{27}	Nϵ2	Gly^{101}	H3	O	2.4
	Gln^{27}	Nϵ2	Asp^{102}	H3	N	3.4
	Gln^{27}	Nϵ2	Asp^{102}	H3	Oδ1	3.0
	Asn^{28}	N	Gly^{101}	H3	O	2.8

Isothermal Titration Calorimetry—Thermodynamic analyses of the interaction between EPR and 9E5 IgG were performed with an iTC200 calorimeter (GE Healthcare). In the calorimeter cell experiment, 9E5 IgG was placed in phosphate-buffered saline (10 mM phosphate buffer (pH 7.4), 150 mM NaCl, and 45 mM KCl) at a concentration of 5 μM, and it was titrated with 100–130 μM EPR solution in the same buffer at 25 °C. The EPR solution was injected 25 times. The thermograms were analyzed with Origin 7 software (GE Healthcare) after subtracting a thermogram measured against only the buffer. The enthalpy change (ΔH) and binding constant (K_A) for the interaction were directly obtained from the experimental titration curve fitted to a one-site binding isotherm. The dissociation constant (K_D) was calculated as $1/K_A$. The Gibbs free energy change ($\Delta G = -RT\ln K_A$) and the entropy change ($\Delta S = (-\Delta G + \Delta H)/T$) for the association were calculated from ΔH and K_A.

SPR Analysis—SPR was carried out to analyze the interaction between 9E5 IgG and hEPR in a Biacore T100 system. Thioredoxin-fused hEPR was immobilized by an amine coupling method at a level of about 124 resonance units on a CM5 sensor chip (GE Healthcare). The binding of 9E5 IgG to hEPR was accomplished by injecting increasing concentration of 9E5 IgG (3.1–50 nM) into the sensor chip under the buffer condition of HEPES-buffered saline with surfactant P20 (pH 7.4) at a flow rate of 30 ml min^{-1} at 25 °C. The data were corrected by subtracting the responses from a blank flow cell in which an amine coupling reaction was carried out. The kinetic parameters and the binding affinity were calculated using the bivalent analyte model with Biacore T100 evaluation software (GE Healthcare).

Results

Complex Structure of 9E5(Fab)·hEPR—We determined the structure of the complex of 9E5(Fab) with hEPR at 2.5-Å resolution (Fig. 1 and Table 1). The asymmetric unit contained one 9E5(Fab)·hEPR complex in a rectangular box with approximate dimensions of 35 × 45 × 90 Å. The interaction between 9E5(Fab) and hEPR formed a solvent-accessible surface of ~919 Å^2, which is in the typical range of interaction surfaces between antibodies and antigens (32).

All six CDRs in 9E5(Fab) (CDR-L1, CDR-L2, and CDR-L3 in the light chain and CDR-H1, CDR-H2, and CDR-H3 in the heavy chain) interacted with hEPR and formed 27 hydrogen bonds or salt bridges as shown in Table 2 with numerous van

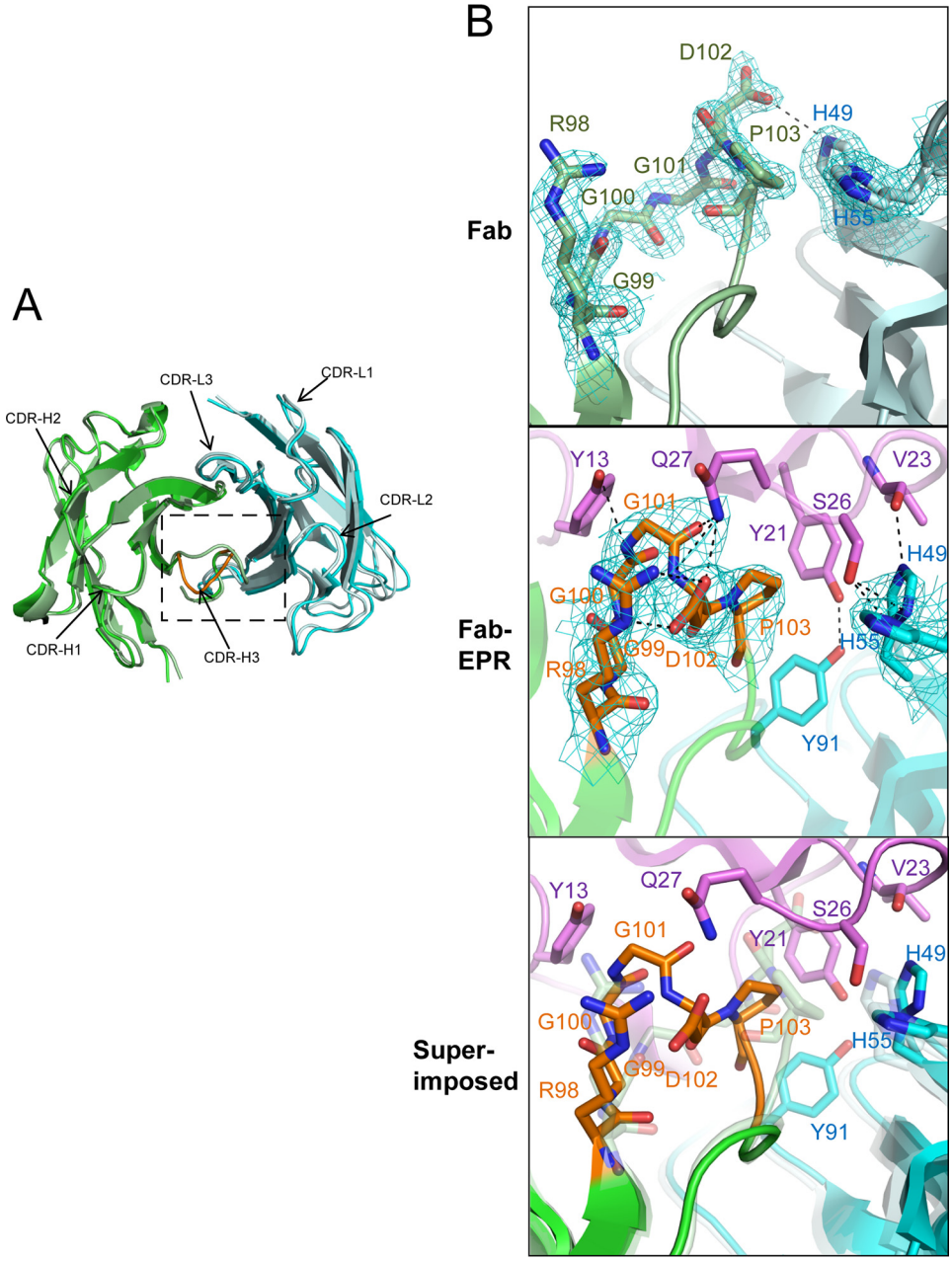

FIGURE 2. **9E5(Fab) fragment superimposed on the 9E5(Fab)·hEPR complex.** *A*, top view of the 9E5(Fab) fragment superimposed on the 9E5(Fab)·hEPR structure. The 9E5(Fab) fragment is shown in the *lighter shade*. The hEPR molecule in the 9E5(Fab)·hEPR complex is omitted in this figure. Drastic change of CDR-H3 is highlighted in *orange*. The r.m.s.d. of the Fv domain (residues 2–117 in the heavy chain and residues 2–14 and 17–104 in the light chain) is 0.9 Å. The noticeable interaction (interaction-3) is indicated by the *black dashed square*. *B*, close-up view of the superimposed structures of 9E5(Fab) with (*solid colors*) and without (*faint colors*) hEPR. 9E5(Fab) (*upper panel*) and 9E5(Fab)·hEPR (*middle panel*) show an electron density map around CDR-H3 and CDR-L2. Each $2F_o - F_c$ electron density map is contoured at 1 σ. In *B*, the orientation corresponds to Fig. 1*E*. *Bottom panel*, 9E5(Fab) fragment superimposed on the 9E5(Fab)·hEPR complex at interaction-3 region.

der Waals interactions. The N-terminal domain of hEPR is recognized by CDR-L1, CDR-L3, and CDR-H2 (Fig. 1*C*). The C-terminal domain of hEPR is stabilized by CDR-H1 and CDR-H2 (Fig. 1*D*). The core region of hEPR (Gly^{E17}–Cys^{E32}; superscript E refers to epiregulin) interacts with CDR-L2 and CDR-H3 (Fig. 1*E*).

We also solved the crystal structure of the 9E5(Fab) fragment at a resolution of 1.6 Å. The superimposition of 9E5(Fab) of the complex on the 9E5(Fab) structure showed relatively small root mean square deviation (r.m.s.d.) values of 0.9 (Fv domain) and 0.7 Å (C_L and C_{H1} domains). The core region of hEPR (residues Gly^{17}–Cys^{32}) also superimposed well on the NMR structure (12) (r.m.s.d., 1.0 Å). Although no dynamic movement of the Fv domain and the core region of hEPR occurs, conformational changes occur in the N- and C-terminal domains in hEPR and in CDR-H3 in 9E5(Fab) (Fig. 2 and Table 2).

Movement of CDR-H3 Induced by hEPR Binding—Interaction-3 is composed of the interaction of CDR-L2 and CDR-H3 with the core region of hEPR (Tyr^{E13}, Tyr^{E21}–Val^{E23}, and Ser^{E26}–Asn^{E28}) (Fig. 1*E*). In interaction-3, little conformational change occurs in hEPR. However, drastic conformational changes occur in CDR-H3 (Fig. 2 and Table 2). The r.m.s.d.

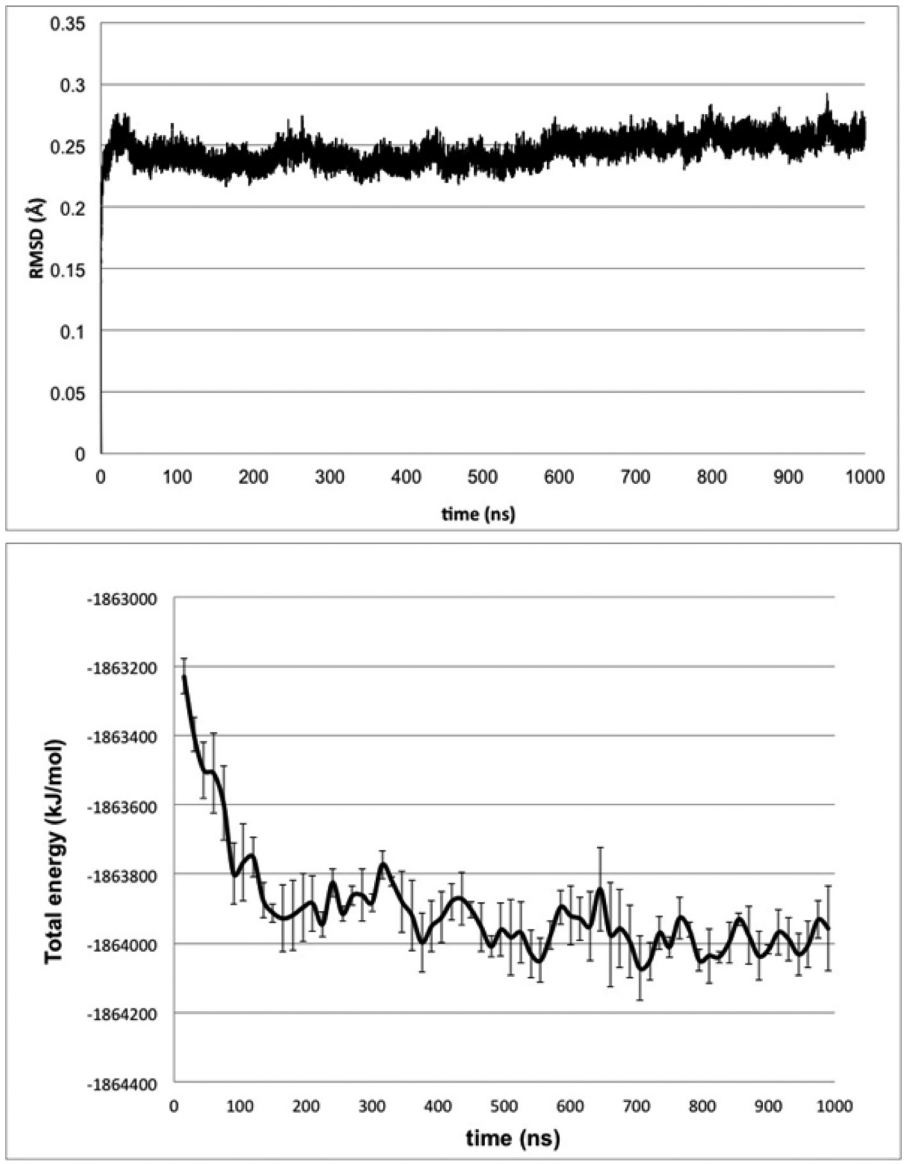

FIGURE 3. **Results from MD simulations of the 9E5(Fab)·hEPR complex.** *A*, r.m.s.d. of the backbone of hEPR and the Fv part of 9E5(Fab) between the simulated structures and the x-ray crystal structure. The r.m.s.d. was averaged for the four simulations. *B*, block averages of the total energy averaged for the four simulations. The block averages were calculated within each 1.5-ns period. The *error bars* indicate the standard errors of the block averages of the four total energies.

value of the Cα atoms of CDR-H3 (Arg^{H98}–Pro^{H103}; superscript H refers to the heavy chain) in the presence or absence of hEPR is 2.4 Å, which is about 2.5 times larger than that of the variable region of the heavy chain (0.9 Å). Asp^{H102} is originally hydrogen-bonded to His^{L49} (superscript L refers to the light chain) in the apo form. However, the hydrogen bond breaks with the insertion of hEPR, resulting in flipping of Asp^{H102} and formation of a new salt bridge with Arg^{H98}. The Cγ carbon in the carboxyl group of Asp^{H102} moves more than 10.8 Å, and the Cα atoms of Gly^{H101} move more than 6.5 Å. A conformational change from cis-Pro^{H103} to trans-Pro^{H103} also occurs upon binding with hEPR. Gly^{H100}, Gly^{H101}, Asp^{H102}, and Pro^{H103} in CDR-H3 form six hydrogen bonds with Tyr^{E13}, Gln^{E27}, and Asn^{E28} (Table 2).

Calculation of the Interaction Energy by Molecular Dynamics—The r.m.s.d. values of hEPR and the Fv part of 9E5(Fab) were compared with the x-ray crystal structure, and the block average of the total energy was calculated from four MD simulations (Fig. 3). The block average was calculated within each 1.5-ns period. Because the system seemed to have reached equilibrium after about 700 – 800 ns (Fig. 3), the binding interactions were analyzed for the trajectories from 900 ns to 1 μs. The interaction energy is defined here as the sum of the short range Lennard-Jones ($r < 0.9$ nm) and coulombic ($r < 1.0$ nm) interactions between the residue pairs, which are the dominant contributions to the binding of hEPR to 9E5(Fab).

Fig. 4 shows the interaction energies of each hEPR residue, which are 100-ns time averages of the equilibrated structures in solution. The solvated structures differed a little from the crystal structure. For example, Table 2 shows that the interaction distance between the carboxyl oxygen atom of Cys^{E6} of hEPR and Oη of Tyr^{L32} of 9E5(Fab) is 3.5 Å in the crystal structure. Although the MD structure provided the shortest O (Cys^{E6})-OH (Tyr^{L32}) distance of 2.6 Å, the longest and time-

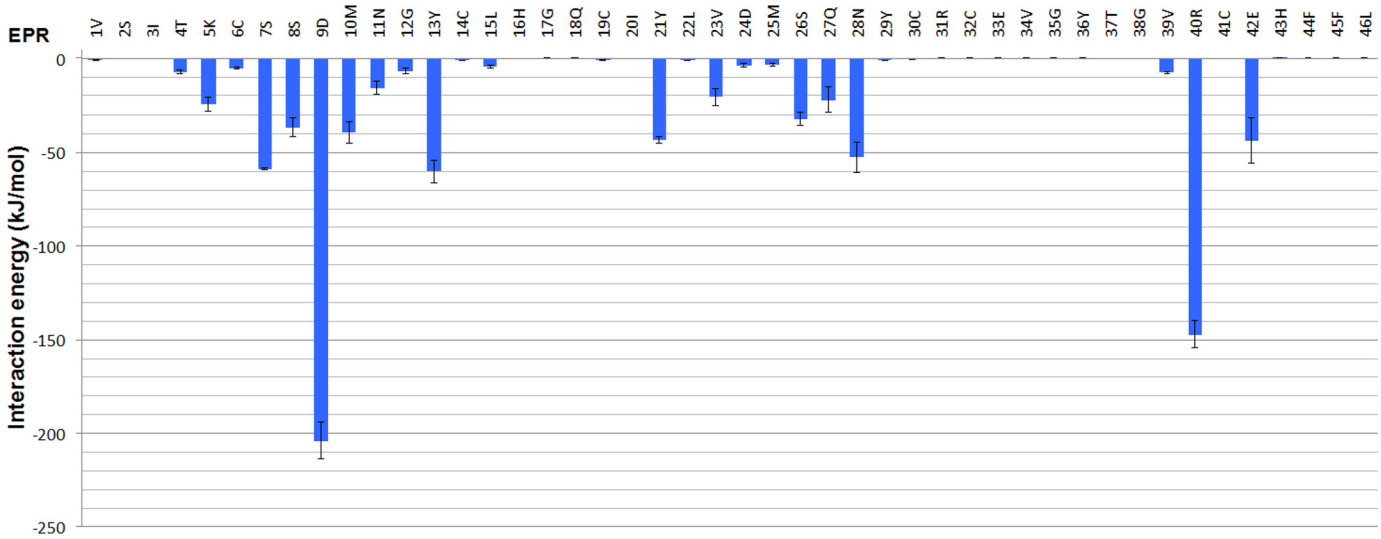

FIGURE 4. **Calculated short range interaction energies of each hEPR residue with 9E5(Fab).** The *error bars* indicate the standard errors of the mean of the four interaction energies averaged over the respective last 100-ns trajectories.

averaged distances were calculated to be 4.0 and 6.8 Å, respectively. This explains why the interaction energy of Cys^{E6} is small in Fig. 4. Asp^{E9} and Arg^{E40} interact with several atoms as shown in Table 2, and all of the distances are greater than 3.0 Å except for Nη1 (Arg^{E40})-Oδ2 (Asp^{H52}) (2.8 Å) (Table 2). However, these residues have the strongest and second strongest interaction energies with 9E5(Fab) in Fig. 4: −204.1 kJ/mol for Asp^{E9} and −147.0 kJ/mol for Arg^{E40}. These residues are located in the regions of interaction-1 and interaction-2, respectively. The hEPR residues in the interaction-3 region moderately interact with CDR-H3 of 9E5(Fab) (−20.7 to −60.3 kJ/mol). The strong interactions of Asp^{E9} and Arg^{E40} cause large conformational changes of hEPR in the interaction-1 and interaction-2 regions.

Table 3 shows the details of the interaction energies of hEPR residues that are greater than −20 kJ/mol in Fig. 4. In the interaction-1 region, Asp^{E9} interacts very strongly not only with Arg^{H50} but also with Arg^{L95}. In the crystal structure, Asp^{E9} (Oδ2) has interaction distances of 3.0 Å with Arg^{H50} (Nη1) and 3.3 Å with Arg^{L95} (Nη2). However, in solution, Asp^{E9} has more stable hydrogen bonds and salt bridges with Arg^{L95} than with Arg^{H50}. Thus, Arg^{L95} has higher interaction energies with Asp^{E9} than with Arg^{H50} in Table 3. In the interaction-2 region, both Arg^{E40} and Glu^{E42} interact with CDR-H1 and CDR-H2 and form strong salt bridges. In the interaction-3 region, seven residues of hEPR (Met^{E10}, Tyr^{E13}, Tyr^{E21}, Val^{E23}, Ser^{E26}, Gln^{E27}, and Asn^{E28}) interact with a total of eight residues of CDR-L2 (His^{L49} and Tyr^{L50}), CDR-H1 (Asp^{H31} and Tyr^{H33}), and CDR-H3 (Gly^{H100}, Gly^{H101}, Asp^{H102}, and Pro^{H103}) in a relatively weak manner. The total interaction energies in the interaction-1, -2, and -3 regions are 290.0, 214.5, and 195.8 kJ/mol, respectively.

Thermodynamic Analyses—To characterize the binding of the antibody to EPR from a thermodynamic viewpoint, we performed ITC analyses of the interaction of 9E5 IgG with EPR wild type (WT) and hEPR and mmEPR mutants (Table 4 and Fig. 5). The mmEPR triple mutant E27Q/K28N/F29Y (m3) was investigated because of the sequential differences between hEPR and mmEPR (Fig. 6).

TABLE 3

Interaction energies of selected residues of EPR with each residue of 9E5(Fab)

The energies are listed for the residues of EPR that are less than −20 kJ/mol in Fig. 4. S.E. indicates the standard error of the mean of four interaction energies averaged over the last 100-ns trajectories.

Interaction part	EPR	9E5(Fab)		Interaction energy (<−4.0 kJ/mol)	
		Residue	CDR	Average	S.E.
				kJ/mol	
Interaction-1	Lys^{5}	Tyr^{32}	L1	−23.5	4.0
	Ser^{7}	Tyr^{32}	L1	−12.2	0.5
		Tyr^{91}	L3	−30.9	0.2
		Asp^{92}	L3	−12.8	0.6
	Ser^{8}	Asp^{92}	L3	−23.2	5.2
		Asn^{93}	L3	−7.5	0.8
	Asp^{9}	Arg^{50}	H2	−44.0	9.0
		Tyr^{91}	L3	−8.8	1.2
		Asp^{92}	L3	−11.0	1.3
		Leu^{94}	L3	−13.9	4.1
		Arg^{95}	L3	−102.2	8.2
Interaction-3	Met^{10}	Tyr^{33}	H1	−10.1	4.8
		Gly^{100}	H3	−4.2	1.5
		Pro^{103}	H3	−5.6	1.7
	Tyr^{13}	Asp^{31}	H1	−24.3	3.7
		Tyr^{33}	H1	−10.9	0.6
		Gly^{100}	H3	−9.1	1.1
		Gly^{101}	H3	−6.4	1.7
	Tyr^{21}	Pro^{103}	H3	−5.5	0.6
		His^{49}	L2	−7.6	1.5
		Tyr^{50}	L2	−9.7	0.7
		Tyr^{91}	L3	−15.3	4.6
	Val^{23}	His^{49}	L2	−5.7	3.0
		Tyr^{50}	L2	−4.6	1.7
	Ser^{26}	Pro^{103}	H3	−5.0	0.6
		His^{49}	L2	−10.6	2.5
		His^{55}	L2	−8.7	3.0
	Gln^{27}	Gly^{101}	H3	−7.1	3.2
		Asp^{102}	H3	−7.4	4.4
		Pro^{103}	H3	−5.0	0.8
	Asn^{28}	Gly^{100}	H3	−18.3	6.2
		Gly^{101}	H3	−16.9	2.2
		Asp^{102}	H3	−7.6	1.7
		Pro^{103}	H3	−9.2	1.5
Interaction-2	Arg^{40}	Asp^{52}	H2	−99.7	3.8
		Leu^{54}	H2	−3.8	0.2
		Lys^{30}	H1	−23.2	7.2
		Asp^{31}	H1	−14.9	5.0
		Thr^{32}	H1	−7.1	1.6
	Glu^{42}	Lys^{30}	H1	−42.3	11.3
		Leu^{54}	H2	−4.9	1.0

hEPR WT showed an exothermic profile, and its binding enthalpy, ΔH, is −8.6 ± 0.7 kcal/mol. The interaction has a strong binding affinity (K_D = 6.5 nM). The hEPR mutant R40A

TABLE 4

Thermodynamic parameters of the interaction of 9E5 IgG with EPR WT and mutants at 25 °C

N, stoichiometry; ND, not detected.

Source	Mutant	N	K_A	K_D	ΔH	$-T\Delta S$	ΔG
			M^{-1}	nM	*kcal/mol*	*kcal/mol*	*kcal/mol*
hEPR	WT	1.90 ± 0.09	16.2 ± 4.9 ×10^7	6.5 ± 2.0	−8.6 ± 0.7	−2.6 ± 1.0	−11.2 ± 0.2
	D9A	2.01 ± 0.04	6.7 ± 0.2 ×10^7	15.0 ± 0.6	−14.0 ± 0.2	3.4 ± 0.2	−10.7 ± 0.1
	S26R	1.92 ± 0.16	2.2 ± 0.8 ×10^7	50.6 ± 18.1	−5.9 ± 0.5	−4.1 ± 0.7	−10.0 ± 0.2
	R40A	ND	ND	ND	ND	ND	ND
mmEPR	WT	ND	ND	ND	ND	ND	ND
	R26S	ND	ND	ND	ND	ND	ND
	m3	1.87 ± 0.10	2.3 ± 0.7 × 10^7	46.4 ± 12.0	−5.0 ± 0.1	−5.0 ± 0.1	−10.0 ± 0.2

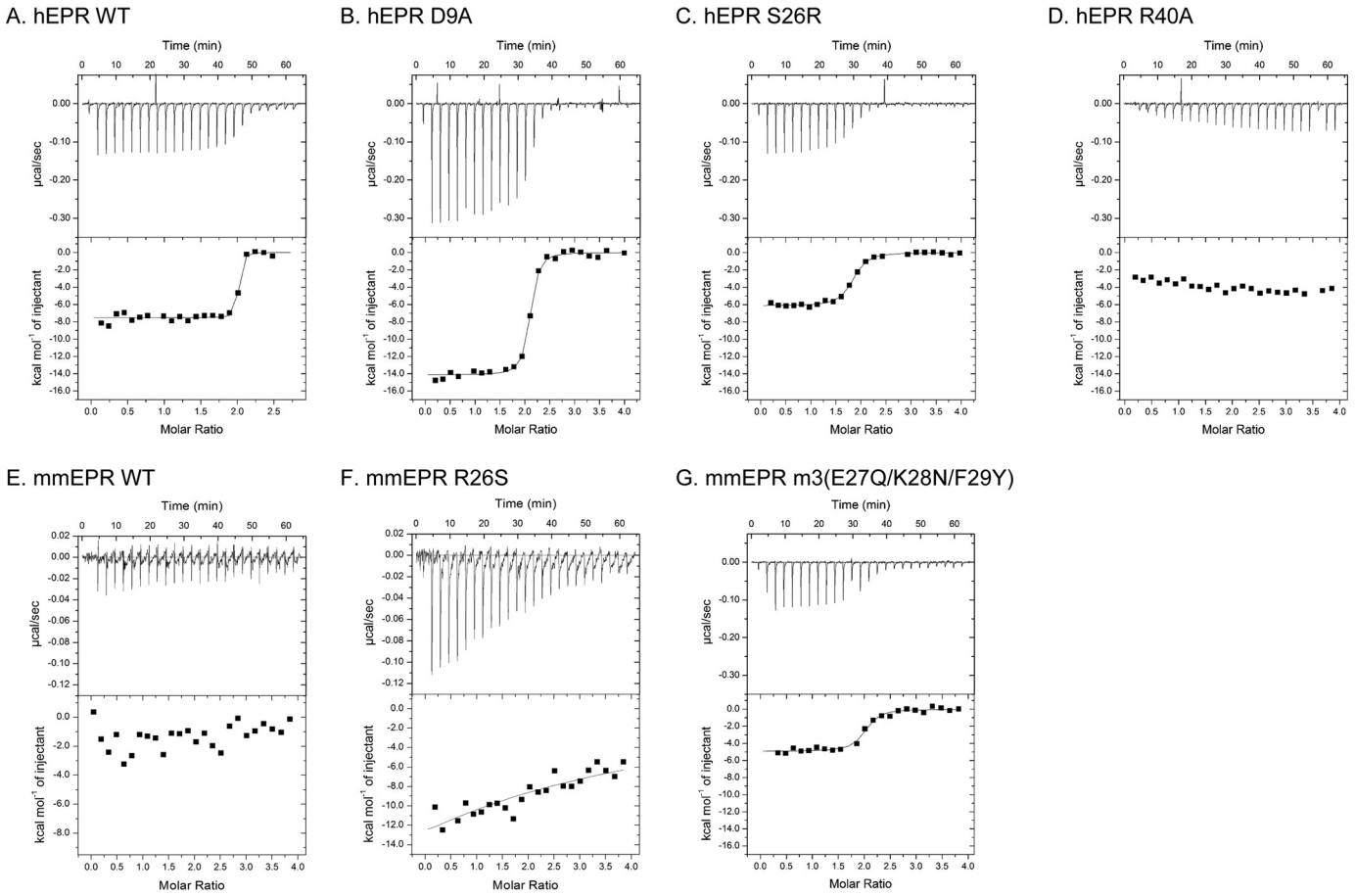

FIGURE 5. **Titration calorimetry of the interaction between 9E5 IgG and EPR.** *A–G*, typical calorimetric titration of 9E5 IgG (5 μM) with 100–130 μM EPR at 25 °C (*top*) and integration plot of the data calculated from the raw data (*bottom*). The *solid line* corresponds to the best fit curve obtained by least square deconvolution. *A*, hEPR WT; *B*, hEPR D9A; *C*, hEPR S26R; *D*, hEPR R40A; *E*, mmEPR WT; *F*, mmEPR R26S; and *G*, mmEPR m3.

showed no heat in the ITC analysis, indicating that Arg^{E40} is one of the hot spot residues in the interaction between hEPR and 9E5 IgG. The other Ala mutant, hEPR D9A, has a lower binding affinity with a large unfavorable entropy change. The binding energy of hEPR S26R is 1.2 kcal/mol higher than that of hEPR WT. These results indicate that steric hindrance or electric repulsion reduces the binding affinity.

As expected, no heat was detected for mmEPR WT. In contrast, mmEPR m3 has a similar binding affinity to S26R hEPR. mmEPR R26S exothermically binds to 9E5 IgG, but the dissociation constant could not be determined because of the weak binding.

SPR Analysis—Kinetic analysis of the interaction between 9E5 IgG and hEPR was carried out by SPR. The sensorgram showed that the dissociation rate of 9E5 IgG is slow (Fig. 7). The kinetic parameters (association rate constant k_{on} and dissociation rate constant k_{off}) were calculated with the bivalent analyte model. The results show that the binding affinity is dominated by the high k_{on} ($k_{on1} = 1.15 \times 10^6\ M^{-1}\ s^{-1}$, $k_{off1} = 9.83 \times 10^{-4}\ s^{-1}$). The K_D value ($=k_{off1}/k_{on1}$) was calculated to be 0.86 nM.

Discussion

In this study, we describe the crystal structures of 9E5(Fab) in the presence and absence of its antigen hEPR. To investigate the recognition mechanism of hEPR by 9E5(Fab), we solved the x-ray structure of 9E5(Fab) with and without hEPR. To bind to hEPR, CDR-H3 undergoes the following three characteristic structural changes (Fig. 2). First is the formation of Asp^{H102}-Arg^{H98} salt bridges. Asp^{H102} in 9E5(Fab) without hEPR forms a hydrogen bond with His^{L49}, thereby contributing to the inter-

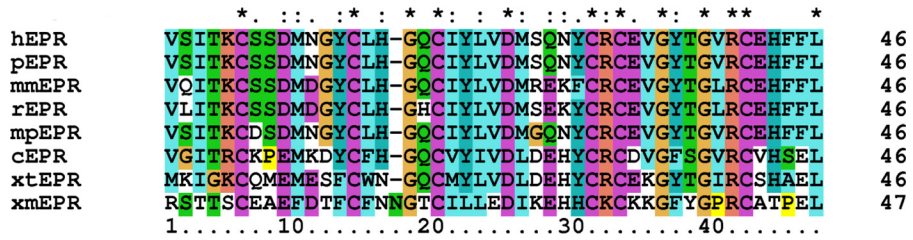

FIGURE 6. **Multiple sequence alignment of the EPRs.** An *asterisk* (*) indicates fully conserved residues. A *colon* (:) indicates strongly similar residues. A *period* (.) indicates weakly similar residues. In mammals, *pEPR*, *rEPR*, and *mpEPR* indicate *Pan troglodytes* (chimpanzee), *Rattus norvegicus* (rat), and *Mustela putorius furo* (European domestic ferret) EPR, respectively. In avian, *cEPR* indicates *Gallus gallus* (chicken) EPR. In amphibian, *xtEPR* indicates *Xenopus tropicalis* (western clawed frog) EPR. In fish, *xmEPR* indicates *Xiphophorus maculatus* (southern platyfish) EPR. The UniProt accession numbers are as follows: hEPR, O14944; pEPR, H2QPP3; mmEPR, Q61521; rEPR, Q9Z0L5; mpEPR, M3YCI3; cEPR, P13387; xtEPR, Q28BU9; and xmEPR, D1MGM2. The alignment and figure drawing were performed using the ClustalΩ and ClustalX programs (39).

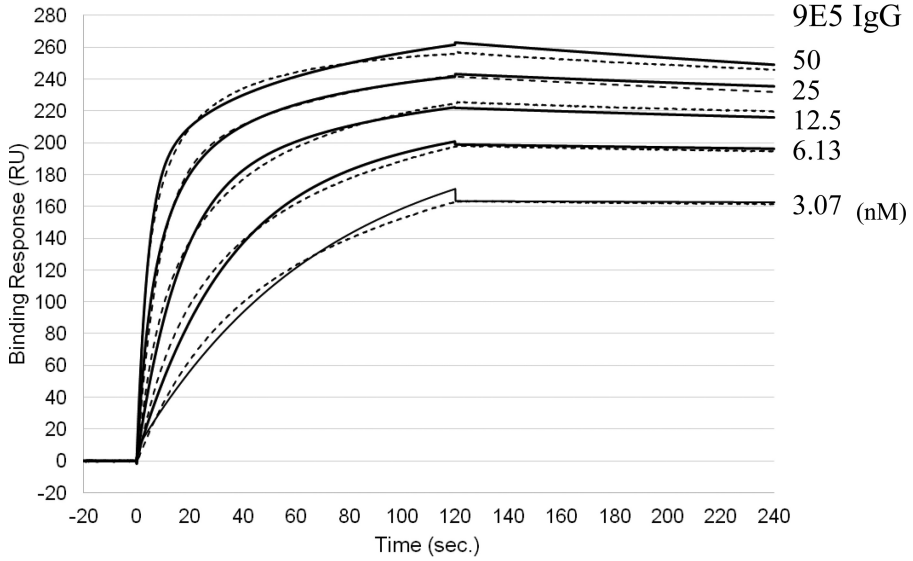

FIGURE 7. **Surface plasmon analysis of the interaction between 9E5 IgG and hEPR.** Thioredoxin-fused hEPR was immobilized by an amine coupling method on a CM5 sensor chip. The analyses were performed by injecting various concentration of 9E5 IgG (3.1–50 nM) into the sensor chip under the buffer condition of HEPES-buffered saline with surfactant P20 (pH 7.4) at a flow rate of 30 ml min^{-1} at 25 °C. *Black dashed lines* show the fitted curves. *RU*, resonance units.

action with CDR-H3 and CDR-L2. The binding of hEPR induces rearrangement of the hydrogen bonds so that Asp^{H102} forms a salt bridge with Arg^{H98}, which was originally exposed to the solvent region, and His^{L49} forms a hydrogen bond with Ser^{E26}. Second are the conformational changes in the Gly^{H99}–Gly^{H101} loop. As described above, Gly^{H101} moves more than 6.5 Å upon binding of hEPR. All of the residues between Arg^{H98} and Asp^{H102} are glycine, and thus proper contact with hEPR is possible because of the flexibility. The third change is cis-trans Pro^{H103} isomerization. In the structure of 9E5(Fab), Pro^{H103} in CDR-H3 is stabilized by hydrophobic interactions with His^{L49} in CDR-L2 and a couple of hydrophobic residues. Although the difference in the energy level between the cis and trans forms is only 2 kJ/mol, the activation energy of cis-trans isomerization is 80–90 kJ/mol (33), meaning that cis-trans isomerization of proline is an energy-requiring reaction.

From the results of the MD simulations, the interaction energy for interaction-3 is relatively small (Fig. 4). However, it is predicted that Asp^{E9} and Arg^{E40} energetically contribute to interaction-1 and interaction-2, respectively. The ITC analysis clearly indicates that D9A hEPR has a comparable binding affinity with hEPR WT, suggesting loss of entropic energy in D9A and the existence of water molecules around Arg^{H50} in the counterpart of 9E5(Fab). It also indicates that Asp^{E9} does not contribute to complex formation. Conversely, the R40A mutant of hEPR does not bind to 9E5 IgG, suggesting that Arg^{E40} is one of the hot spots for 9E5 IgG (Table 4). This interaction energy may contribute to cis-trans isomerization. The formation of a salt bridge between Asp^{H102} and Arg^{H98} may also contribute to cis-trans isomerization. Once these conformational changes have occurred, it may not be able to return to the structure of CDR-H3, suggesting that the 9E5(Fab)·hEPR complex is difficult to dissociate without some type of energy, such as thermal energy. In fact, SPR analysis indicates that the rate of dissociation is extremely slow (Fig. 7). It is concluded that 9E5(Fab) is an effective antibody against hEPR because 9E5(Fab) strongly binds to hEPR and cannot easily dissociate.

9E5(Fab) can only recognize hEPR, and it can be called a *human trap* antibody. We will now discuss the specific recognition by 9E5(Fab) from the viewpoint of the amino acid alignment of hEPR (Fig. 6). Ser^{E26}–Tyr^{E29} in hEPR interacts- with CDR-H3 in 9E5(Fab), corresponding to Arg^{E26}–Phe^{E29} in mmEPR. The results of ITC analysis indicate that the K_D value of the S26R mutant of hEPR is about 7 times higher than that of WT (Table 4). In contrast, the binding affinity of mmEPR m3 is on the order of 10^{-8} M. These results suggest that all of the Ser^{E26}–Phe^{E29} sequence in hEPR is essential for the specific recognition of 9E5(Fab).

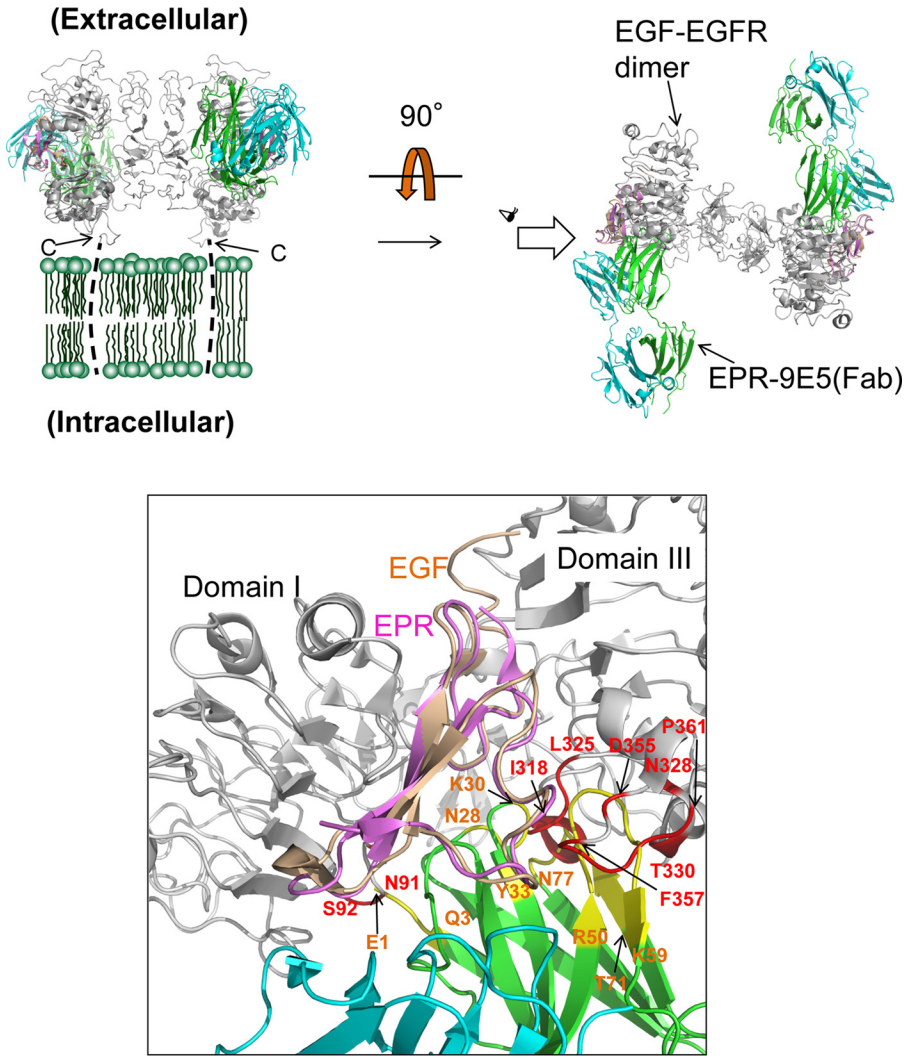

FIGURE 8. **Superimposed structures of 9E5(Fab)·hEPR and EGF·EGFR complexes.** The *upper panel* shows hEPR in the 9E5(Fab)·hEPR complex (*colored*) superimposed on EGF in the EGF-EGFR complex (*gray*; Protein Data Bank code 1IVO). The *lower panel* shows a close-up view around the binding site of EGFR indicated by the *arrow* in the *upper panel*. EGF is *wheat-colored*. The r.m.s.d. between hEPR and EGF is 0.9 Å. The EGFR residues within 2 Å of the hEPR residues are shown in *red*. The 9E5(Fab) residues within 2 Å of EGFR are shown in *yellow*.

EPR specifically binds to the homodimers of EGFR, ErbB-1, and ErbB-4 (34, 35). To date, three structures of ligands of the EGF family complexed with the EGFR ectodomain have been reported: EGF·ErbB-1 (Protein Data Bank code 1IVO), transforming growth factor α (TGFα)·ErbB-1 (Protein Data Bank code 1MOX), and neuregulin1β·ErbB-4 (Protein Data Bank code 3U7U) (36–38). To investigate how to accomplish binding of 9E5(Fab)·hEPR to EGFR, we superimposed 9E5(Fab)·hEPR on the EGF·ErbB-1 ectodomain (Fig. 8). hEPR in EPR-9E5(Fab) superimposed well on EGF in EGF·ErbB-1, and the average r.m.s.d. between 40 Cα atom pairs was 0.9 Å. The light chain of 9E5(Fab) does not interact with ErbB-1 and EGF. However, the heavy chain of the N-terminal region (Glu^{1}–Gln^{3}), CDR-H1 ($Asn^{H}28$–$Lys^{H}30$ and $Tyr^{H}33$), CDR-H2 ($Arg^{H}50$–$Lys^{H}59$), and the region from the β7 sheet to the η3 3^{10} helix ($Thr^{H}71$–$Asn^{H}77$) in 9E5(Fab) interact with Domain I (Tyr^{88} and Asn^{91}–Ser^{92}) and Domain III (Ile^{318}–Leu^{325}, Asn^{328}, Thr^{330}, Asp^{355}, and Phe^{357}–Pro^{361}) in ErbB-1. For this reason, the interactions of the heavy chain of 9E5(Fab) prevent binding of the complex of 9E5(Fab)·hEPR to ErbB-1. This tendency is almost the same as TGFα·ErbB-1 and NRG1β·ErbB-4 complexes (37, 38). Therefore, 9E5(Fab)-captured hEPR could not bind to ErbB-1 and ErbB-4.

From the viewpoint of kinetics, the K_D values of 9E5 IgG and hEPR WT are 0.86–6.5 nM, which were observed by ITC and SPR analysis (Fig. 7 and Table 4). hEPR is a much weaker antagonist of the ErbB-1 and ErbB-4 receptors with IC_{50} values of 2800 nM and >5 μM, respectively (34), indicating that 9E5 IgG binds to hEPR more strongly than ErbB-1 and ErbB-4. According to previous studies, mutational analysis and chemical regeneration suggest that the guanidinium group of Arg^{E40} in hEPR is essential for binding of the ErbB receptor (40, 41). These results support that 9E5(Fab) acts as not only the simple capturer of EPR but also the competitive neutralization antibody against EGFR with inhibition of the functional residue Arg^{E40}.

In conclusion, 9E5(Fab) binds to only hEPR with rearrangement of the hydrogen bonding network along with cis-trans isomerization of Pro^{H103} and shows high affinity and slow dissociation. MD simulation and ITC analyses uncovered that

Arg^{E40} acts as a hot spot in the interaction between hEPR and 9E5 IgG. Antibody drugs based on the structure of 9E5 with the conservation of the human trap recognition mechanism are expected, especially for colon cancer.

Author Contributions—M. I., Y.-H. L., and Y. S. prepared 9E5(Fab); Y. K., A. S., T. M., and T. N. constructed EPR expression plasmids; Y. K., E. M., T. N., and T. Y. purified EPR or EPR-9E5(Fab) complex; Y. K., E. M., T. Y., H. M., and T. I. performed X-ray crystallography; S. N., T. M., and K. T. performed thermodynamic analyses; K. S., H. D., and H. F. performed molecular dynamics simulations; T. Kawamura determined 9E5 sequence by proteomics analysis; Y. K. wrote the manuscript with input from all the coauthors; E. M., T. I., and T. Kodama conceived and designed the study; and T. Kodama supervised the Molecular Dynamics for Antibody Drug Development project.

Acknowledgments—We are grateful to Reiko Satoh, Kyoko Watanabe, and Maiko Nampo for support with cultivation, purification, and crystallization. We express appreciation to Dr. Eiki Yamashita, Dr. Atsushi Nakagawa (SPring-8 beam-line 44XU), and Dr. Naohiro Matsugaki (Photon Factory beam-line 5A) for support with data collection.

References

1. Nielsen, D. L., Kümler, I., Palshof, J. A., and Andersson, M. (2013) Efficacy of HER2-targeted therapy in metastatic breast cancer. Monoclonal antibodies and tyrosine kinase inhibitors. *Breast* **22,** 1–12
2. Sahin, U., Weskamp, G., Kelly, K., Zhou, H. M., Higashiyama, S., Peschon, J., Hartmann, D., Saftig, P., and Blobel, C. P. (2004) Distinct roles for ADAM10 and ADAM17 in ectodomain shedding of six EGFR ligands. *J. Cell Biol.* **164,** 769–779
3. Hynes, N. E., and Lane, H. A. (2005) ERBB receptors and cancer: the complexity of targeted inhibitors. *Nat. Rev. Cancer* **5,** 341–354
4. Yarden, Y., and Sliwkowski, M. X. (2001) Untangling the ErbB signalling network. *Nat. Rev. Mol. Cell Biol.* **2,** 127–137
5. Fischer, O. M., Hart, S., Gschwind, A., and Ullrich, A. (2003) EGFR signal transactivation in cancer cells. *Biochem. Soc. Trans.* **31,** 1203–1208
6. Yu, H., and Jove, R. (2004) The STATs of cancer—new molecular targets come of age. *Nat. Rev. Cancer* **4,** 97–105
7. Baba, I., Shirasawa, S., Iwamoto, R., Okumura, K., Tsunoda, T., Nishioka, M., Fukuyama, K., Yamamoto, K., Mekada, E., and Sasazuki, T. (2000) Involvement of deregulated epiregulin expression in tumorigenesis *in vivo* through activated Ki-Ras signaling pathway in human colon cancer cells. *Cancer Res.* **60,** 6886–6889
8. Révillion, F., Lhotellier, V., Hornez, L., Bonneterre, J., and Peyrat, J. P. (2008) ErbB/HER ligands in human breast cancer, and relationships with their receptors, the bio-pathological features and prognosis. *Ann. Oncol.* **19,** 73–80
9. Freimann, S., Ben-Ami, I., Hirsh, L., Dantes, A., Halperin, R., and Amsterdam, A. (2004) Drug development for ovarian hyper-stimulation and anticancer treatment: blocking of gonadotropin signaling for epiregulin and amphiregulin biosynthesis. *Biochem. Pharmacol.* **68,** 989–996
10. Tørring, N., Hansen, F. D., Sørensen, B. S., Ørntoft, T. F., and Nexø, E. (2005) Increase in amphiregulin and epiregulin in prostate cancer xenograft after androgen deprivation-impact of specific HER1 inhibition. *Prostate* **64,** 1–8
11. Lee, Y. H., Iijima, M., Kado, Y., Mizohata, E., Inoue, T., Sugiyama, A., Doi, H., Shibasaki, Y., and Kodama, T. (2013) Construction and characterization of functional anti-epiregulin humanized monoclonal antibodies. *Biochem. Biophys. Res. Commun.* **441,** 1011–1017
12. Sato, K., Nakamura, T., Mizuguchi, M., Miura, K., Tada, M., Aizawa, T., Gomi, T., Miyamoto, K., and Kawano, K. (2003) Solution structure of epiregulin and the effect of its C-terminal domain for receptor binding affinity. *FEBS Lett.* **553,** 232–238
13. Moulin, A., Mathieu, M., Lawrence, C., Bigelow, R., Levine, M., Hamel, C., Marquette, J. P., Le Parc, J., Loux, C., Ferrari, P., Capdevila, C., Dumas, J., Dumas, B., Rak, A., Bird, J., Qiu, H., Pan, C. Q., Edmunds, T., and Wei, R. R. (2014) Structures of a pan-specific antagonist antibody complexed to different isoforms of TGFβ reveal structural plasticity of antibody-antigen interactions. *Protein Sci.* **23,** 1698–1707
14. Otwinowski, Z., and Minor, W. (1993) in *Proceedings of the CCP4 Study Weekend, Data Collection and Processing* (Sawyer, L., Issacs, N., and Bailey, S., eds) pp. 56–62, Science and Engineering Research Council (England), Daresbury Laboratory, Warrington, UK
15. Staelens, S., Hadders, M. A., Vauterin, S., Platteau, C., De Maeyer, M., Vanhoorelbeke, K., Huizinga, E. G., and Deckmyn, H. (2006) Paratope determination of the antithrombotic antibody 82D6A3 based on the crystal structure of its complex with the von Willebrand factor A3-domain. *J. Biol. Chem.* **281,** 2225–2231
16. McCoy, A. J. (2007) Solving structures of protein complexes by molecular replacement with Phaser. *Acta Crystallogr. D Biol. Crystallogr.* **63,** 32–41
17. Emsley, P., and Cowtan, K. (2004) Coot: model-building tools for molecular graphics. *Acta Crystallogr. D Biol. Crystallogr.* **60,** 2126–2132
18. Murshudov, G. N., Skubák, P., Lebedev, A. A., Pannu, N. S., Steiner, R. A., Nicholls, R. A., Winn, M. D., Long, F., and Vagin, A. A. (2011) REFMAC5 for the refinement of macromolecular crystal structures. *Acta Crystallogr. D Biol. Crystallogr.* **67,** 355–367
19. Afonine, P. V., Grosse-Kunstleve, R. W., Echols, N., Headd, J. J., Moriarty, N. W., Mustyakimov, M., Terwilliger, T. C., Urzhumtsev, A., Zwart, P. H., and Adams, P. D. (2012) Towards automated crystallographic structure refinement with phenix.refine. *Acta Crystallogr. D Biol. Crystallogr.* **68,** 352–367
20. Brünger, A. T. (1992) Free R value: a novel statistical quantity for assessing the accuracy of crystal structures. *Nature* **355,** 472–475
21. Lovell, S. C., Davis, I. W., Arendall, W. B., 3rd, de Bakker, P. I., Word, J. M., Prisant, M. G., Richardson, J. S., and Richardson, D. C. (2003) Structure validation by Cα geometry: ϕ,ψ and Cβ deviation. *Proteins* **50,** 437–450
22. DeLano, W. L. (2006) *The PyMOL Molecular Graphics System*, version 0.99rc6, Schrödinger, LLC, New York
23. Van Der Spoel, D., Lindahl, E., Hess, B., Groenhof, G., Mark, A. E., and Berendsen, H. J. (2005) GROMACS: fast, flexible, and free. *J. Comput. Chem.* **26,** 1701–1718
24. Hess, B., Kutzner, C., van der Spoel, D., and Lindahl, E. (2008) GROMACS 4: algorithms for highly efficient, load-balanced, and scalable molecular simulation. *J. Chem. Theory Comput.* **4,** 435–447
25. Pronk, S., Páll, S., Schulz, R., Larsson, P., Bjelkmar, P., Apostolov, R., Shirts, M. R., Smith, J. C., Kasson, P. M., van der Spoel, D., Hess, B., and Lindahl, E. (2013) GROMACS 4.5: a high-throughput and highly parallel open source molecular simulation toolkit. *Bioinformatics* **29,** 845–854
26. Fujitani, H., Matsuura, A., Sakai, S., Sato, H., and Tanida, Y. (2009) High-level ab initio calculations to improve protein backbone dihedral parameters. *J. Chem. Theory Comput.* **5,** 1155–1165
27. Nose, S. (1984) A molecular-dynamics method for simulations in the canonical ensemble. *Mol. Phys.* **52,** 255–268
28. Hoover, W. G. (1985) Canonical dynamics: equilibrium phase-space distributions. *Phys. Rev. A* **31,** 1695–1697
29. Parrinello, M., and Rahman, A. (1981) Polymorphic transitions in single crystals—a new molecular-dynamics method. *J. Appl. Phys.* **52,** 7182–7190
30. Hess, B., Bekker, H., Berendsen, H. J. C., and Fraaije, J. G. E. M. (1997) LINCS: a linear constraint solver for molecular simulations. *J. Comput. Chem.* **18,** 1463–1472
31. Darden, T., York, D., and Pedersen, L. (1993) Particle mesh Ewald—an N·log(N) method for Ewald sums in large systems. *J. Chem. Phys.* **98,** 10089–10092
32. Davies, D. R., and Cohen, G. H. (1996) Interactions of protein antigens with antibodies. *Proc. Natl. Acad. Sci. U.S.A.* **93,** 7–12
33. Brandts, J. F., Halvorson, H. R., and Brennan, M. (1975) Consideration of the possibility that the slow step in protein denaturation reactions is due to cis-trans isomerism of proline residues. *Biochemistry* **14,** 4953–4963

34. Jones, J. T., Akita, R. W., and Sliwkowski, M. X. (1999) Binding specificities and affinities of egf domains for ErbB receptors. *FEBS Lett.* **447,** 227–231
35. Komurasaki, T., Toyoda, H., Uchida, D., and Morimoto, S. (1997) Epiregulin binds to epidermal growth factor receptor and ErbB-4 and induces tyrosine phosphorylation of epidermal growth factor receptor, ErbB-2, ErbB-3 and ErbB-4. *Oncogene* **15,** 2841–2848
36. Ogiso, H., Ishitani, R., Nureki, O., Fukai, S., Yamanaka, M., Kim, J. H., Saito, K., Sakamoto, A., Inoue, M., Shirouzu, M., and Yokoyama, S. (2002) Crystal structure of the complex of human epidermal growth factor and receptor extracellular domains. *Cell* **110,** 775–787
37. Garrett, T. P., McKern, N. M., Lou, M., Elleman, T. C., Adams, T. E., Lovrecz, G. O., Zhu, H. J., Walker, F., Frenkel, M. J., Hoyne, P. A., Jorissen, R. N., Nice, E. C., Burgess, A. W., and Ward, C. W. (2002) Crystal structure of a truncated epidermal growth factor receptor extracellular domain bound to transforming growth factor α. *Cell* **110,** 763–773
38. Liu, P., Cleveland, T. E., 4th, Bouyain, S., Byrne, P. O., Longo, P. A., and Leahy, D. J. (2012) A single ligand is sufficient to activate EGFR dimers. *Proc. Natl. Acad. Sci. U.S.A.* **109,** 10861–10866
39. Sievers, F., Wilm, A., Dineen, D., Gibson, T. J., Karplus, K., Li, W., Lopez, R., McWilliam, H., Remmert, M., Söding, J., Thompson, J. D., and Higgins, D. G. (2011) Fast, scalable generation of high-quality protein multiple sequence alignments using Clustal**Ω**. *Mol. Syst. Biol.* **7,** 539
40. Engler, D. A., Campion, S. R., Hauser, M. R., Cook, J. S., and Niyogi, S. K. (1992) Critical functional requirement for the guanidinium group of the arginine 41 side chain of human epidermal growth factor as revealed by mutagenic inactivation and chemical reactivation. *J. Biol. Chem.* **267,** 2274–2281
41. Defeo-Jones, D., Tai, J. Y., Vuocolo, G. A., Wegrzyn, R. J., Schofield, T. L., Riemen, M. W., and Oliff, A. (1989) Substitution of lysine for arginine at position 42 of human transforming growth factor-α eliminates biological activity without changing internal disulfide bonds. *Mol. Cell. Biol.* **9,** 4083–4086